Enhanced Photoelectrochemical Performance of Atomic Layer Deposited Hf-doped ZnO

Boulos Alfakes [a,b]†, Corrado Garlisi [c]†, Juan Villegas [d], Abdulrahman Al-Hagri [a,b], Srinivasa Tamalampudi [a,b], Nitul S. Rajput [a,b], Jin-You Lu [a,b], Erik Lewin [e], Jacinto Sá [e,f], Ibraheem Almansouri [a], Giovanni Palmisano [c] and Matteo Chiesa [a,b,g]**

[a] Laboratory for Energy and NanoScience (LENS), Khalifa University of Science and Technology, Masdar Campus, Abu Dhabi 54224, UAE

[b] Department of Mechanical and Materials Engineering, Khalifa University of Science and Technology, Masdar Campus, Abu Dhabi 54224, UAE

[c] Department of Chemical Engineering, Khalifa University of Science and Technology, Masdar Campus, Abu Dhabi 54224, UAE

[d] Department of Electrical and Computer Engineering, New York University, Abu Dhabi 129118, UAE

[e] Department of Chemistry – Ångström Laboratory, Uppsala University, 75 120 Uppsala, Sweden

[f] Institute of Physical Chemistry – Polish Academy of Sciences, 01-224 Warsaw, Poland

[g] Department of Physics and Technology, UiT The Arctic University of Norway, N-9037 Tromsø, Norway

† Both authors contributed equally to this work.

* matteo.chiesa@ku.ac.ae

* giovanni.palmisano@ku.ac.ae

Abstract

Generation of hydrogen using photoelectrochemical (PEC) water splitting has attracted researchers for the last two decades. Several materials have been utilized as an anode in a water splitting cell, including ZnO due to its abundance, low production cost and suitable electronic structure. Most research attempts focused on doping ZnO to tailor its properties for a specific application. In this work, atomic layer deposition (ALD) was used to precisely dope ZnO with hafnium (Hf) in order to enhance its PEC performance. The resultant doped materials showed a significant improvement in PEC efficiency compared to pristine ZnO, which is linked directly to Hf introduction revealed by detailed optical, structural and electrical analyses. The photocurrent obtained in the best performing Hf-doped sample (0.75 wt.% Hf) was roughly threefold higher compared to the undoped ZnO. Electrochemical impedance spectroscopy (EIS) and open-circuit potential-decay (OCPD) measurements confirmed suppression in photocarriers' surface recombination in the doped films, which led to a more efficient PEC water oxidation. The enhanced PEC performance of Hf-doped ZnO and effectiveness of the used metal dopant are credited to the synergistic optimization of chemical composition, which enhanced the electrical, structural including morphological, and optical properties of the final material, making Hf-doping an attractive candidate for novel PEC electrodes.

1. Introduction:

Hydrogen generation enabled through photoelectrochemical (PEC) splitting of water is a recognized approach to providing a sustainable, storable alternative for fossil fuels. A PEC cell utilizes a semiconductor/electrolyte junction to absorb solar photons with energy larger than the band gap of the semiconductor, generating electron hole pairs (EHPs). These EHPs are separated by the built-in electric field. Consequently, the separated holes and electrons contribute to the oxidation and reduction reactions of water, producing O_2 and H_2, respectively [1, 2]. It is worth mentioning that concomitant and complete consumption of electron and holes is paramount for an active and stable photosystem.

1 The requirement for a stable material in such oxidant-rich conditions established the trend for metal
2 oxides to be used as the semiconductor anode in a PEC cell. Common and highly studied materials are TiO_2
3 [3-6], Fe_2O_3 [7-10], and WO_3 [11]. ZnO is another promising metal oxide that has been employed in various
4 applications, including transistors [12, 13], light emitting devices [14, 15], photovoltaics [16-18],
5 biosensors [19-21], and photo-catalytic applications due to its material abundance, low production cost, and
6 low toxicity. As a result, researchers have used different methods to produce ZnO for water splitting
7 purposes, such as hydrothermal, electrochemical, spray pyrolysis, sol-gel and sputtering [22, 23], with a
8 preference for nanorods and nanowires over thin films, due to their larger surface area and short lateral
9 carrier diffusion length [24, 25]. However, ZnO suffers from photocorrosion under UV irradiation [26-28]
10 and in aqueous media, which raises the need for combining it with other materials to overcome this
11 deficiency.

12 Even though few research articles have investigated atomic layer deposition (ALD) grown ZnO for
13 water splitting, ALD provides a method of depositing other materials that can be combined with ZnO to
14 enhance light trapping and/or the durability of the semiconductor electrode [29-34]. In addition, ALD
15 allows highly controlled, reproducible and, most importantly, conformal growth, due to the self-limiting
16 nature of its reaction [35], which provides excellent coverage of highly performing 3D structures in water
17 splitting applications [36]. Furthermore, this type of self-limiting reaction enables precise control over
18 doping of the deposited layers. Doping has been extensively utilized to improve the PEC performance of
19 ZnO, providing a facile and effective approach for modification of its properties, including surface area,
20 crystallinity, surface defects and band gap energy [23, 24, 37-45].

21 Hf doping of ZnO (HZO) presents a relatively new but promising dopant due to the high tunability
22 it grants to the ZnO electrical and optical properties [46-49]. Previously, we have studied this material for
23 application in solar cells, where it proved to be a worthy candidate [49]. However, there is only a single
24 study reporting the enhancement of the photocatalytic activity of ZnO following Hf doping [47]. Here, Hf-
25 doped ZnO, in form of powder, has been tested for the degradation of water contaminants, revealing an

increased photoactivity compared to bare ZnO due to a high visible light absorption and the tendency of Hf to act as a reservoir for the photogenerated electrons. However, to the best of our knowledge, the effect of this dopant on water splitting PEC performance has yet to be reported.

Herein, we report the impact of Hf doping of ZnO on its PEC response, prepared by ALD method. A detailed optical, electrical, structural and photochemical characterization is carried out, providing an insight into how different doping concentrations alter the physicochemical properties of ZnO, and eventually its PEC activity.

2. Materials and methods:

Hf-doped ZnO films, of different doping concentrations, were deposited using an Oxford FlexAL ALD system. ZnO was deposited using Diethyl-zinc (DEZ) and H_2O as precursors, while Hf doping was added using tetrakis-ethylmethylaminohafnium (TEMAH), and H_2O vapor. The amount of doping was varied by changing the cycle ratio of TEMAH+ H_2O cycles to DEZ + H_2O cycles. The deposition pressure and temperature were 200 mTorr and 250 °C, respectively. Briefly, the deposition was performed on three different substrates, fluorine doped tin oxide (FTO) coated glass, UV transparent fused silica slides, and <100> p-type Si. The fused quartz slides were used to measure optical transmission and reflection using a Shimadzu UV-2600 spectrophotometer over the range of 200 to 900 nm. Also, films grown on quartz were used to measure X-ray diffraction (XRD) using a Malvern Panalytical Empyrean X-ray diffractometer with Cu Kα radiation, and Bragg-Brentano geometry to perform θ/2θ -scans. The obtained peaks were fitted to a Voigt function, to calculate the d-spacing using Bragg's law.

The chemical composition of the HZO films grown on Si was analyzed through X-ray photoelectron spectroscopy (XPS), using an Ulvac-Phi Quantera II instrument with monochromatic Al Kα radiation and a 45° photoelectron take-off angle. Measurements were conducted under constant charge neutralization using low energy Ar^+ and electrons [50]. Sputter depth profiles through the HZO thin films were acquired using 1 keV Ar^+ rastered over 1x1 mm area, and the chemical composition calculated as an

1 average through three depths within the thin film, using sensitivity factors provided by the instrument
2 manufacturer.

3 A standard *in-situ* lift-out procedure was implemented to prepare lamellae for the
4 Scanning/Transmission Electron Microscopy (S/TEM) analysis [51]. The lamellae were prepared in a dual-
5 beam FIB system (Thermo Fisher Scientific, Helios 650). As part of the fabrication process, a capping layer
6 of Pt was deposited using the available precursor gas $(CH_3)_3Pt(CpCH_3))$ in the dual-beam system. For the
7 TEM and STEM study, an image corrected TEM system (Thermo Fisher Scientific, Titan G2) operating at
8 300 kV was utilized. The tool has an X-field emission gun (X-FEG) source that provides a high quality
9 electron beam. The system is equipped with analytical components such as, Energy Dispersive
10 Spectroscopy (EDS) for elemental analysis, and a Gatan Imaging Filter (GIF Quantum SE) for energy
11 filtered TEM (EFTEM) and electron energy loss spectroscopy (EELS) studies.

12 Photoelectrochemical (PEC) analyses were performed using a three-electrode cell connected to a
13 potentiostat/galvanostat (Metrohm Autolab PGSTAT302N). HZO films deposited on FTO, platinum and
14 Ag/AgCl electrodes were used as working, counter and reference electrodes, respectively. The electrolyte
15 was 0.5 M Na_2SO_4 (pH 5.6). Photocurrent transients were recorded at a potential of 0.6 V vs. NHE.
16 Electrochemical impedance spectroscopy (EIS) was performed in the frequency range of 0.1 Hz – 10 kHz
17 with an applied potential of 0.6 V vs. NHE. Mott-Schottky (MS) experiments were performed under 10
18 kHz with potential step of 50 mV. For measurements performed under UV/Vis light, samples were
19 irradiated with a 250 W mercury UV lamp connected to an optical fiber. The average values of the
20 irradiance reaching the sample surface, measured with a DeltaOhm 9721 radiometer, were 96, 205, 146 and
21 373 W m^{-2} in the 200-280, 280-315, 315–400 and 450–950 nm ranges, respectively.

3. Results and discussion:

3.1 Chemical Composition

The number of cycles used, doping weight acquired from XPS analyses, and deposition thickness obtained from cross-sectional images (not shown) for HZO films under study are summarized in Table 1.

Table 1 Deposition parameters, average Hf weight percentage for two sets of samples, and obtained thickness for HZO films under study

Cycle ratio (Hf: ZnO)	**0:1**	**1:9**	**1:4**	**1:1**
Hf weight percentage (wt.%)	Not detected	0.67 ± 0.12	0.75 ± 0.13	1.70 ± 0.28
Number of cycles	350	400	460	740
Thickness obtained (nm)	72	78	78	85

XPS analyses of the Hf 4f region clearly show an increase in Hf content with increase of Hf: ZnO cycle ratio, and no Hf signal in the undoped ZnO film. Observed doping is in the range of 0.00 - 0.42 at.% (0 - 1.70 wt.%), without apparent linear dependence between the concentration and the number of cycles. The relatively low intensity of Hf 4f creates some uncertainty in the estimation of Hf concentration. A possible explanation for the absence of a trend could be a non-uniform dopant distribution through the films. From the high-ratio film (1:1), it seems that Hf is present at higher concentrations close to the interface with the substrate but always with the same oxidation state (Figure S1).

Figure S2 and S3 show the XPS analyses of the Zn 2p region for the pristine ZnO and HZO with high-ratio (1:1) films. The signal was fitted using a doublet ration separation of 23.1 eV [52, 53] and constrains for the area and peak width. The signal was fitted with a single component with the Zn $2p_{3/2}$ signal maximum centered at 1022 eV consisting Zn in the form of ZnO [54, 55]. It is worth noting that the

1 signal for the HZO did not change after a couple of sputtering cycles, suggesting that Hf concentration is
2 never high enough to perturb the Zn electronic structure significantly throughout the entire film.

3 Figure S4 shows the XPS analysis of the Hf 4f region for the HZO with high-ratio (1:1) films. The
4 signal was fitted using a doublet ration separation of 1.68 eV [56] and constrains for the area and peak
5 width. The signal was fitted with a single component with the Hf $4f_{7/2}$ signal maximum centered at 17.5 eV
6 consistent with Hf in +4 oxidation state [57]. It is worth noting that the Hf 4f signal position in the HZO
7 film did not change after a couple of sputtering cycles despite the noticeable increase in Hf concentration,
8 suggesting that Hf is present as Hf^{4+} throughout the entire film independently of its concentration.

9 3.2 Structural and morphological properties

10 Figure 1 presents the XRD patterns of the four samples deposited on fused silica. Diffraction peaks
11 are in good agreement with the reference patterns for hexagonal wurtzite ZnO (JCP2.2CA 01-079-2205),
12 which confirms that all HZO films consist of this phase [58]. The presence of (100), (002) and (101)
13 reflections reveal the polycrystalline nature of the samples, while the highest intensity of the (002)
14 orientation indicates that crystals are mainly composed of exposed (002) crystalline planes, resulting in a
15 preferential growth along the *c*-axis perpendicular to the substrate [59, 60]. In comparison for films grown
16 on a Si substrate, the presence of the (101) peak at 36.3° can be observed, in addition to the weaker signal
17 intensity [49]. Nevertheless, similar to films deposited on Si, it is evident that the (002) peak intensity is
18 increasing with doping, indicating a more columnar growth. Furthermore, it can be seen in Table S1 that
19 the lattice constants are not significantly altered with doping, due to the close radius of Hf^{4+} (0.78 Å) to the
20 radius of Zn^{2+} (0.74 Å) [61-64], confirming effective substitution in this range of low doping concentrations.

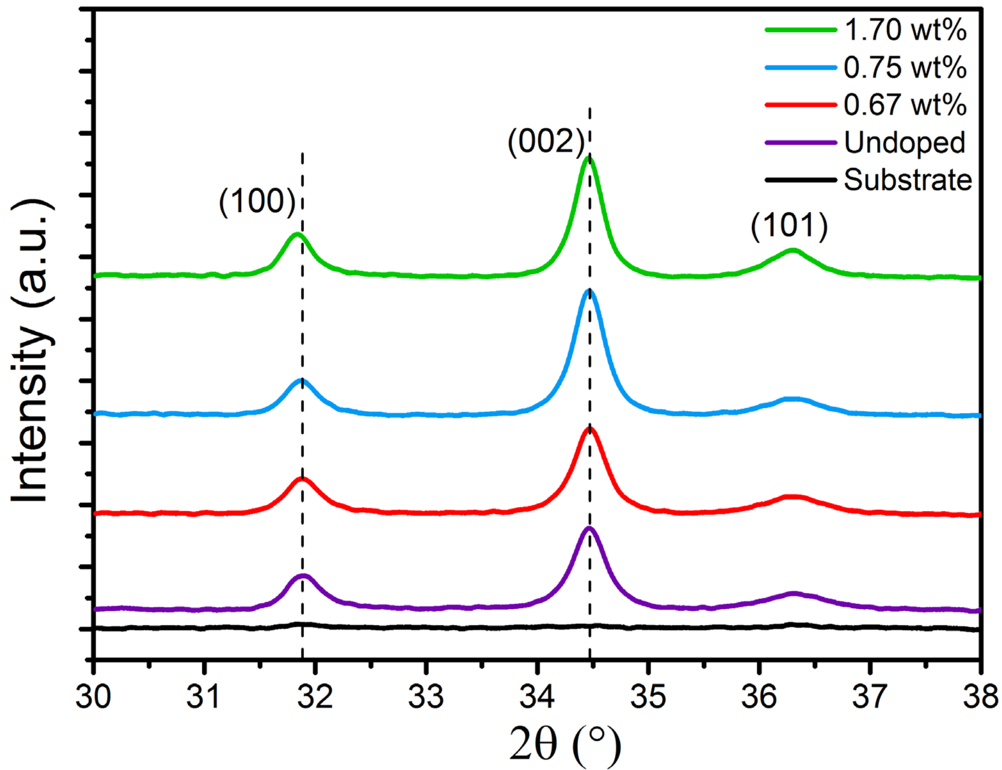

1

2 *Figure 1 XRD pattern measured on fused silica substrates for different HZO film.*

3

4 SEM measurements corroborate this observation through the detected change of morphology of the
5 films with doping. Figure S5 shows the evolution of the wedge-shaped microstructure in the undoped ZnO
6 film into a columnar microstructure for the 1.70 wt% doped film, corresponding to (100) and (002) facets,
7 respectively [65].

1

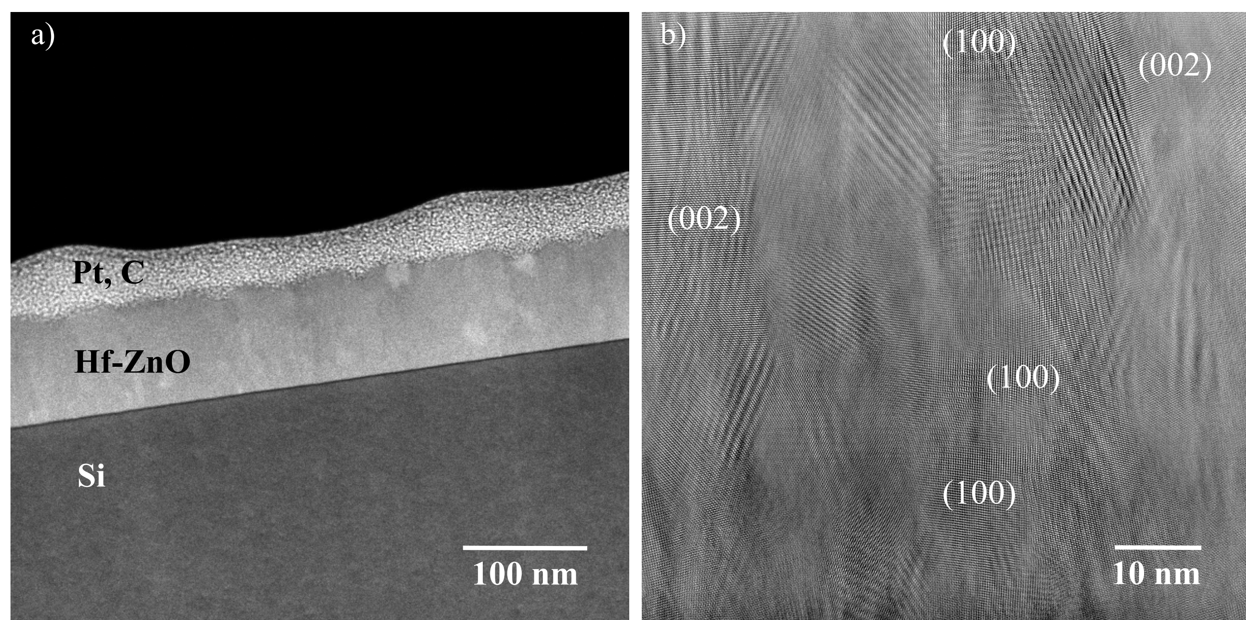

2 *Figure 2 (a) A low magnification HAADF STEM image acquired from the prepared lamella. (b) A HRTEM image*
3 *collected from the Hf-doped ZnO film (1.70 wt%).*

4 A low magnification cross-sectional view of the grown material (1.70 wt%) is shown in Figure 2a.
5 Thickness of the deposited layer, as deduced from the high angle angular dark field (HAADF) STEM
6 images, is found to be 85 nm. As can be seen in the images, no visible cracks or pores were observed.
7 EFTEM images were collected from a selected region of the lamella and are shown in Figure S6. This
8 indicates a homogeneous distribution of Zn and O. However, given the low concentration of Hf, Hf-edges
9 due to core losses could not be observed in the EELS spectrum. Furthermore, high-resolution TEM
10 (HRTEM) images are acquired from the doped ZnO film (Figure 2b). TEM investigations indicated the
11 presence of a high degree of polycrystallinity, mostly dominated by (002) and (100) planes. In addition, no
12 visible amorphous region was observed and the nanocrystalline regions were found to mostly be in
13 columnar shape.

14 In the context of water splitting, Pawar et al. studied the effect of ZnO crystal facets on the PEC
15 performance [66]. A higher photocurrent for anodes with (002) facet was obtained in comparison to the
16 (100) and (101) anodes, due to the fact that the (002) facets possess lower charge resistance at the interface

with the electrolyte. This facet engineering, mainly higher (002) facet exposure as a result of Hf doping, agrees well with our photoelectrochemical results below.

3.3 Optical properties

From the transmission and reflection spectra of the HZO films (shown in S7), the absorption coefficient was obtained through the following equation:

$$\alpha = -\frac{1}{d} \ln \frac{T}{1-R} \quad (1)$$

Subsequently, the band gap was obtained using Tauc method, in which the band gap energy can be determined through the intercept of the linear region of the $(\alpha h\nu)^{1/n}$ curve with the photon energy (hν) x-axis [67, 68], as shown in Figure 3a.

$$(\alpha h\nu)^{1/n} \propto (h\nu - E_g) \quad (2)$$

Where α is the absorption coefficient, h is Planck's constant, ν is the photon frequency, and E_g is the optical band gap. n has a value of ½ for direct band gap materials. Urbach energy (E_U) is another parameter that can be obtained from the absorption coefficient values near the band edge through equation (3) [69].

$$\alpha \propto \exp\left(\frac{h\nu}{E_U}\right) \quad (3)$$

This equation characterizes the optical transitions between occupied states in the band tail of the valence band to unoccupied states of the conduction band edge. Urbach energy is obtained through the reciprocal of the slope of $\ln \alpha$ in the linear region of the curve, as shown in Figure 3b. Results of the E_g and E_U are presented in Table 2. The Urbach energy is increasing from 61 meV for the undoped film to 100 meV for the 1.70 wt% film. This agrees with the commonly reported increase in Urbach energy as a result of doping in ZnO [34, 70, 71], and implies the increase of the width of the localized states in the band gap.

1 The broadening of the Urbach tails, along with an increase in E_g from 3.30 eV in the undoped
2 sample to 3.46eV in 1.70 wt% sample, is indicative of a rearrangement of the band structure in doped films
3 with a larger number of transitions from band to tail and tail to tail [71, 72]. The role of mid-gap states on
4 the semiconductor photoresponse is not consensual. On the one hand, they can undermine the
5 photoresponse, acting as recombination centers for the photocarriers, while on the other they can improve
6 it, acting as further absorption centers, which can compensate for the intrinsic limitation of wide band-gap
7 semiconductors in visible-light harvesting [73-75]. In addition to optical properties, other factors such as
8 electrical and structural features' impact on the PEC performance are discussed further on.

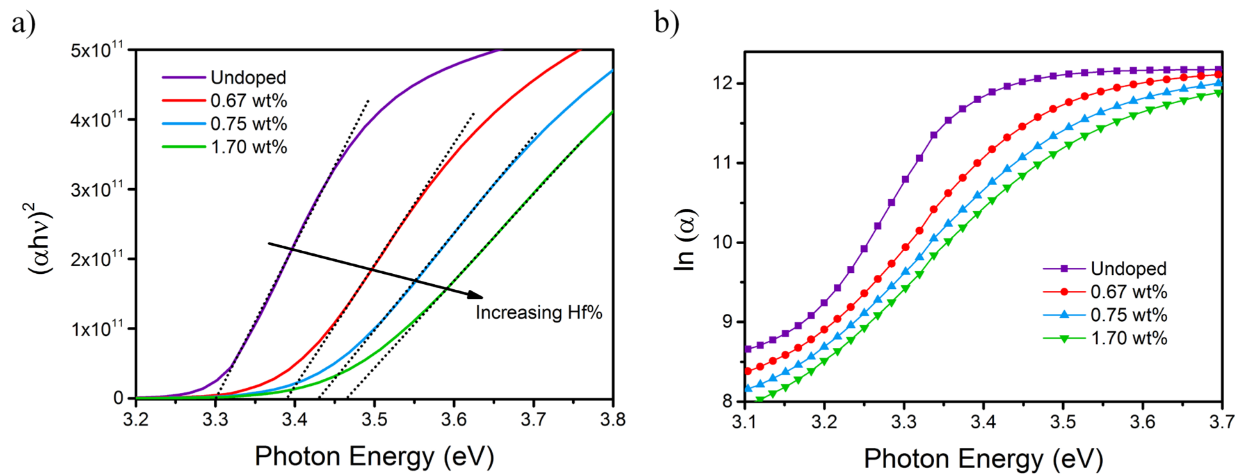

9

10 *Figure 3 a) Tauc plot and b) Urbach plot for different films.*

11 The majority of research attempts for improving ZnO anode performance focused on narrowing its
12 band gap, to shift its absorption peak towards visible wavelengths. This results in higher charge carrier
13 generation [24, 38, 76], but also a reduction of the material redox window, i.e., band edge redox power.
14 Doping with Hf clearly increases its band gap, shifting its absorption further into the ultraviolet (up to 3.46
15 eV), i.e., limited absorption range. Furthermore, Figure 3b also shows that the absorption coefficient
16 decreases on increasing Hf-doping, creating electrodes highly suitable to work as transparent conductive
17 oxide (TCO), but vaticinating lower photocurrents for anodes doped with Hf. Contrary to expectations, the
18 Hf doping increases the generated photocurrent by roughly threefold comparatively to the undoped anode,
19 as shown further on. PEC performance is governed by the complex interaction between optical, electrical

and structural properties. Therefore, doping with Hf changes the ZnO structural properties, including exposed facet, and enhances electrical properties to outweigh the drawbacks of band gap expansion observed.

3.4 Photoelectrochemical properties

MS plots were obtained to measure the flat band potential (EFB) and donor density (ND) in the space charge region, which can be extracted from the x-intercept and the slope of the plot (Figure 4). The capacitance (C) of the space charge region can be related to the applied voltage (E) through the following equation:

$$\frac{1}{C^2} = \frac{2}{\varepsilon_0 \varepsilon e N_D}\left(E - E_{FB} - \frac{kT}{e}\right) \tag{4}$$

Where ε_0 is the vacuum permittivity, $\varepsilon = 10$ is the permittivity of ZnO, e is the electronic charge, T is the temperature (ca. 298 K) and k is the Boltzmann constant. The positive slope of the MS plots confirmed the n-type nature of pure ZnO and Hf-doped ZnO. Doping increased N_D and caused a negative shift of the E_{FB}, decreasing from -0.158 in undoped to -0.299 V vs. NHE in the 1.70 wt% sample (Table 2). A more cathodic E_{FB} is usually indicative of two main factors: (i) higher separation efficiency of the photogenerated carriers; (ii) upward-shift of the Fermi level and, in general, a more favorable energy level shifting against water redox potential [77, 78]. In compact, thin films with a relatively flat surface, like the ones under investigation, the conduction band edge (E_C) differs only very slightly from E_{FB}. Therefore, it can be assumed that E_C and E_{FB} are roughly equal and the valence band edge (E_V) can be determined from E_{FB} and E_g (Table 2) [73, 79]. Notably, all the doped samples showed a valence band edge lowering, denoting stronger oxidation ability from their holes and thus a larger driving force for water oxidation compared to pure ZnO. Doping also caused a marked rise in the donor density, increasing from 1.96 x 10^{19} in undoped film to 4.5 x 10^{19} cm^{-3} in 1.70 wt% doped one. The presence of electron donors responsible for the n-type conductivity in pure ZnO is usually ascribed to oxygen vacancies [80, 81]. On the other hand, the

1 proliferation of donor impurities with increasing doping may result from Hf^{4+} ions and boosting of further
2 oxygen vacancies, which support the population of the conduction band and the Burstein Moss shift. It is
3 believed that increasing N_D is beneficial for PEC properties of semiconductor materials. However, high
4 doping levels may also lead to degeneracy and increased charge recombination, causing an adverse PEC
5 performance [63].

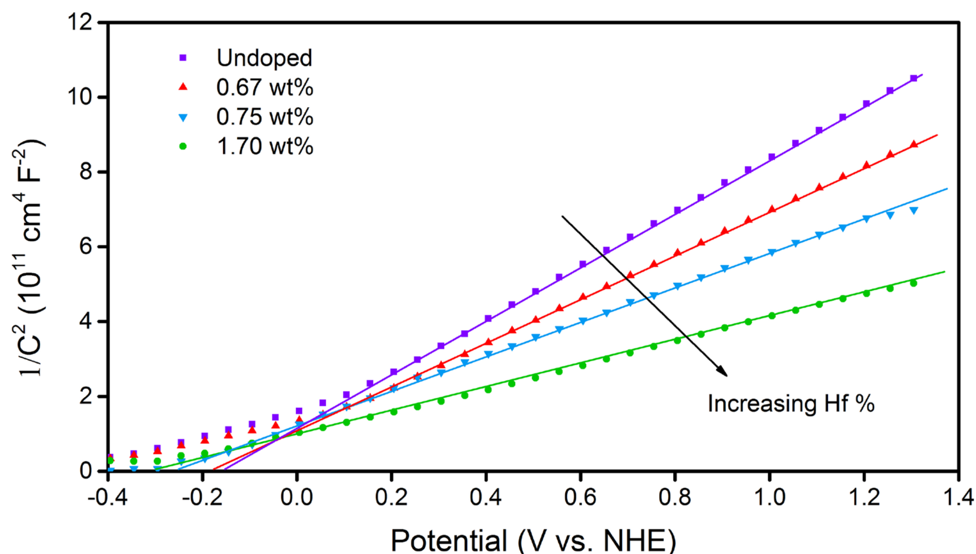

6

7 *Figure 4 MS plots for HZO thin films prepared with different Hf concentrations.*

8 Amperometric measurements were carried out to investigate the photoresponse of the different
9 films over time. Figure 5a displays the photocurrent transients at 0.6 V vs. NHE obtained during on/off
10 illumination cycles under UV irradiation. All the samples exhibited an anodic stationary photocurrent with
11 spikes of the same sign, indicative of an n-type behaviour. Undoped ZnO and 0.67 wt% doped films had
12 similar steady-state photocurrent densities (J) of 2.2 and 2.6 μA cm^{-2}, respectively, while 0.75 wt% film
13 showed remarkably enhanced performance, with J about 2.5 times higher than that in pure ZnO. This
14 suggests that low Hf doping (i.e. 0.75 wt%) significantly improves the charge separation and, consequently,
15 the PEC activity. However, a further increase in Hf content (i.e. 1.70 wt%) did not result in any
16 improvement, due to the increase in recombination centres introduced by Hf atoms. This can be further

understood through examining previously reported mobility values for those films [49]. It is observed that mobility decreases with doping, due to impurity scattering. The direct proportionality of diffusivity with mobility, also known as Einstein relation, also implies that films with higher mobility will have large diffusion length, potentially allowing more photogenerated carrier to contribute to the extracted current. Thus, the enhancement of photocurrent with doping reaches a limit where the low mobility of generated carriers becomes dominant, resulting in higher recombination rate. The solar to chemical conversion efficiency (η) was obtained by equation (5), after measuring the photocurrent J at different applied voltages (E) [73, 82].

$$\eta = \frac{J(1.23 - E)}{I_{light}} \quad (5)$$

Where I_{light} is the power density of the incident light. As shown in Figure S8, the 0.75 wt% sample showed the highest efficiency (0.11%), almost four times time higher than that of undoped ZnO (0.03%).

Figure 5b shows the Nyquist plots of the EIS measurements, aiming to study the kinetics of charge transfer between the HZO films and electrolyte. The inset of the same figure displays the equivalent model for a double capacitor used for fitting the EIS data. Such a model includes an ohmic resistance in series with two RC circuits [63, 73, 79-81, 83]. The series resistance R_s takes into account the electrolyte resistance, external contact resistance and FTO substrate; R_1 and the constant phase element CPE_1 accounts for the resistance and capacitance in semiconductor bulk/depletion layer (high-frequency contribution), while R_2 and CPE_2 represent the charge transfer resistance at the semiconductor/electrolyte interface and Helmholtz capacitance, respectively (low-frequency contribution). No significant changes were observed in R_1, indicating a similar charge transfer in the bulk/depletion layer in all the samples. On the other hand, R_2 values were significantly different, suggesting a strong impact of the doping on the kinetics at the film/electrolyte interface. R_2 values are summarised in Table 2. The trend was consistent with the photocurrent transients: (i) the film with 0.75 wt% doping was the sample with the lowest R_2, resulting in the smallest arc radius in the Nyquist plot; (ii) undoped and 0.67 wt% samples exhibited similar charge

1 transfer resistance; (iii) above a certain threshold, the doping did not improve the charge transfer as shown

2 by the 1.70 wt% doped sample. It can be said, therefore, that moderate Hf-doping benefits the PEC activity,

3 as demonstrated by the 0.75 wt% doped sample, which allowed faster kinetics of the redox reaction at the

4 thin-film surface. The lowest charge transfer impedance is the result of the high (002) orientation leading

5 to more reactive catalytic sites in the material. Furthermore, an increased (002) facet exposure can also

6 enhance the surface hydrophilicity, facilitating the supply of redox species to the electrode and,

7 consequently, the PEC performance. Indeed, a (002) facet is a Zn-rich facet, where surface Zn atoms possess

8 one dangling bond, which is responsible for the enhanced surface energy and thus hydrophilicity [66].

a)

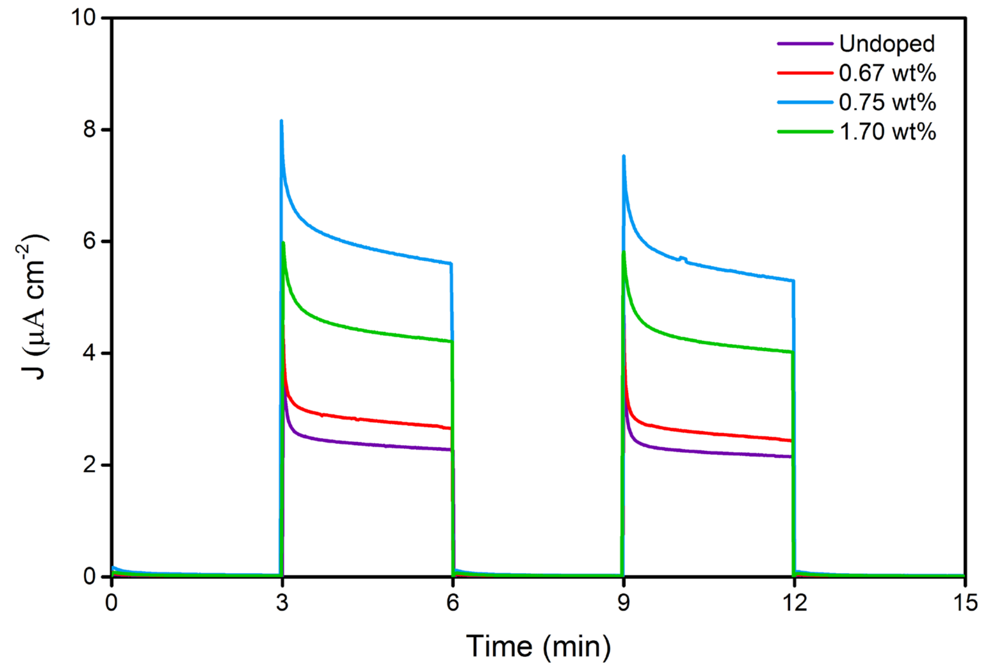

b)

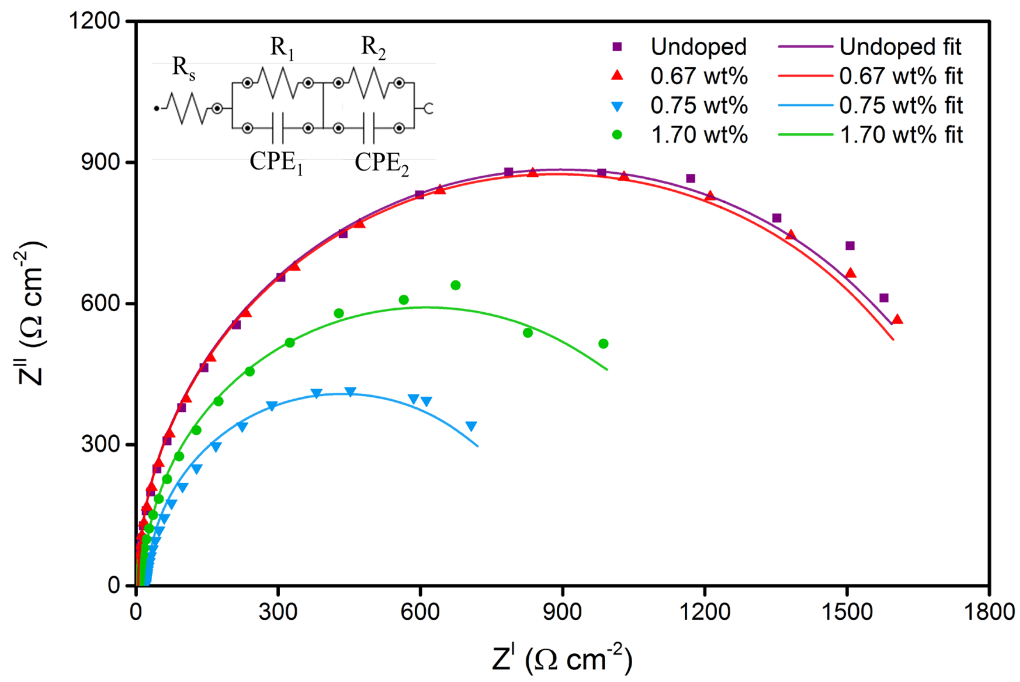

1

2 *Figure 5 (a) Photocurrent transients at 0.6 V vs. NHE and (b) Nyquist plots for HZO samples.*

3

1 The surface recombination process was investigated by open-circuit potential-decay (OCPD)
2 measurements, in order to gain a better insight into the dissimilar charge transfer kinetics revealed by the
3 different HZO samples. In Figure 6, the normalized OCPD curves obtained by relaxation upon interruption
4 of the illumination are displayed for the various samples. The OCP is related to the difference between the
5 Fermi level in the semiconductor and the Pt counter electrode [84]. In dark condition, this difference
6 depends on the redox equilibrium. Under UV irradiation, due to the hole scavenging by H_2O at the
7 film/electrolyte interface, the electrons accumulate within HZO. This leads to a shift in the Fermi level, and
8 therefore in the OCP, to more negative potentials. The OCP thus reaches a steady-state value at which
9 charge recombination and electron accumulation are competing. After interrupting the illumination, the
10 VOC shows a decay dictated by the recombination phenomena of the electrons by surface trapped holes
11 and their scavenging by acceptor species in the electrolyte [85]. However, the OCP decay usually occurs in
12 the time domain of few minutes, while charge recombination in lattice bulk of ZnO is a fast process (ns-μs
13 domain). This implies that the OCPD can be mainly related to the recombination between the redox species
14 in the electrolyte and surface trapped charges [86].

15 The OCPD constant can be seen as a pseudo first-order constant k_r, and can be calculated by fitting
16 the exponential decay during relaxation using the following equation:

$$\frac{E_t - E_{ph}}{E_0 - E_{ph}} = 1 - \exp(-k_r t) \tag{6}$$

17

18 Where E_t is the OCP at any time t, while E_{ph} and E_0 are the steady-state OCP values under UV irradiation
19 and in dark condition, respectively. The values of k_r for the different samples are summarized in Table 2.
20 Undoped and 0.67 wt% doped films showed similar recombination, while the OCPD was significantly
21 retarded in 0.75 wt% and 1.70 wt% films. In particular, 0.75 wt% sample exhibited the lowest k_r, meaning
22 that the water oxidation by the holes is more effective than in the other samples. As a consequence, the
23 accumulated electrons in the films survive longer resulting in a slower decay. This proves that Hf-doping
24 suppresses the formation of surface states, which act as recombination centres for the photogenerated

1 carriers, and determine a more inefficient water oxidation by the holes (i.e. higher k_r) in pure and lightly

2 doped ZnO. However, high doping levels preclude a further improvement of the PEC performance, as found

3 in 1.70 wt% doped film, likely due to the emergence of new surface states in the materials.

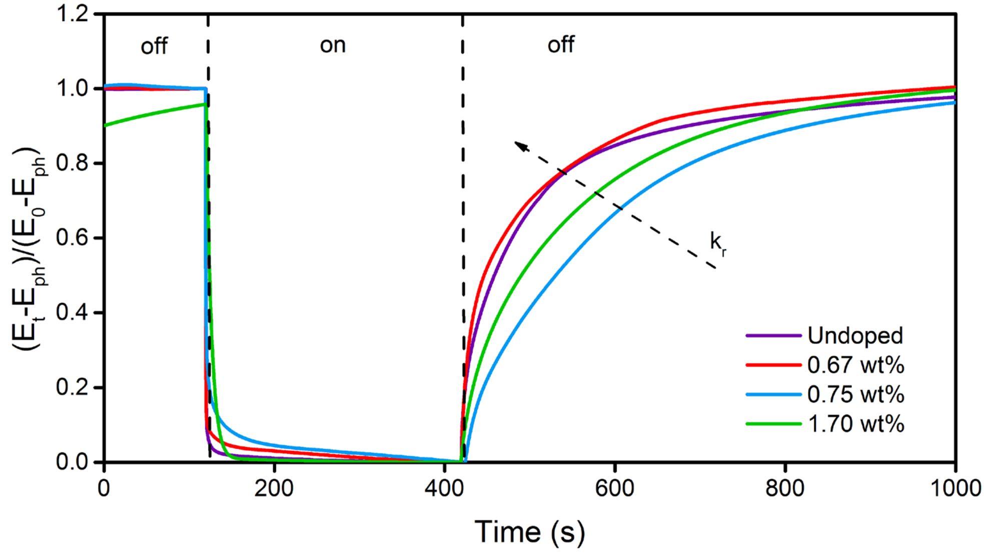

4

5 *Figure 6 Normalized OCPD curves for HZO samples.*

6

7 *Table 2 E_g, E_u, E_{FB}, E_C, E_V, N_D, R_2, K_r values for HZO samples*

Sample	**E_g (eV)**	**E_U (meV)**	**$E_{FB} \approx E_C$ (V vs. NHE)**	**E_V (V vs. NHE)**	**N_D x 10^{19} (cm^{-3})**	**R_2 (Ω cm^{-2})**	**k_r x 10^{-2} (s^{-1})**
Undoped	3.30	61	-0.158 ± 0.006	3.142 ± 0.006	1.96 ± 0.07	1778 ± 20	1.28 ± 0.08
0.67 wt%	3.39	85	-0.175 ± 0.005	3.215 ± 0.005	2.38 ± 0.05	1761 ± 17	1.47 ± 0.08
0.75 wt%	3.43	97	-0.252 ± 0.007	3.178 ± 0.007	3.05 ± 0.08	822 ± 21	0.63 ± 0.06
1.70 wt%	3.46	100	-0.299 ± 0.002	3.161 ± 0.002	4.50 ± 0.09	1194 ± 25	0.82 ± 0.02

8

3.5 Photostability

To study the photostability of Hf-doped ZnO, both optical and structural properties for films deposited on FTO were measured before and after the PEC experiment. Figure S9 present the XRD diffractogram and optical transmittance of ZnO film deposited on an FTO substrate, before and after the PEC runs. The results show that the ZnO film post-experiment exhibits similar behaviour to the FTO substrate, optically and structurally. This is indicative of the occurrence of corrosion phenomena during the PEC tests, agreeing with literature for the low stability of ZnO in aqueous solution [27, 87]. However, repeated runs confirmed that the anode exhibits a stable performance throughout the photocurrent transient and OCPD measurements. This observation suggests that the instability of the material may be triggered at a later stage by the potential and frequency sweeps set in EIS and MS experiments, which cause the HZO films to partly dissolve and corrode in the electrolyte. This limitation is also observed for other anode candidate materials [27, 88]. The aforementioned phenomenon stresses the need for a high conformity deposition technique such as ALD, to combine the highly promising doped ZnO with more stable films, such as TiO_2 in a single reactor. In this regard, Lui et al. utilized ALD to create an ultra-thin shell of TiO_2 over ZnO nanowires, combining the enhanced electronic properties of ZnO (in comparison to TiO_2) and the high stability of TiO_2 [32]. Similarly, Li et al. employed ALD to deposit a Ta_2O_5 protective layer on ZnO NR photoanodes, achieving a praiseworthy stability of 5 hours [89].

4. Conclusion

In this work, ALD grown Hf-doped ZnO was studied as a semiconductor photoanode for water splitting applications. A low doping concentration (i.e. 0.75 wt%) is found to be sufficient for improvement of the PEC performance, resulting in a photocurrent threefold higher than undoped ZnO. This is attributed to a good balance between carrier concentration and mobility, higher (002) facet exposure, along with a marked reduction of recombination centers, ensuring faster charge transfer kinetics at the electrode-electrolyte interface.

This research, in addition to proving the viability of utilizing ALD Hf-doped ZnO films for water splitting applications, also proposes Hf doping of ZnO using other deposition methods and/or other structures, such as nanowires or nanorods. In this respect, ALD Hf-doped ZnO may be grown on appropriate templates and/or combined with more porous materials in order to increase the effective surface area of the electrode.

Finally, a monolithic approach, in which ALD technique can be used to introduce further materials in the photoanode, coupling unstable highly active Hf-doped ZnO with an appropriate protective layer, is an attractive option to overcome the aforementioned limitations of those films before its practical application in water photosplitting.

Acknowledgement

The author would like to thank Dr. Cyril Aubry, Dr. Thomas Delclos, and Mr. Leslie George from Khalifa University for their continuous assistance. Further thanks are extended to Dr. Latifa Yousef for proofreading of the manuscript. M.C. acknowledges the support of the Arctic Center for Sustainable Energy (ARC), UiT Arctic University of Norway through grant no. 310059.

References:

[1] M. Grätzel, nature, 414 (2001) 338.
[2] O. Khaselev, J.A. Turner, Science, 280 (1998) 425-427.
[3] S.U. Khan, M. Al-Shahry, W.B. Ingler, science, 297 (2002) 2243-2245.
[4] M. Ni, M.K. Leung, D.Y. Leung, K. Sumathy, Renewable and Sustainable Energy Reviews, 11 (2007) 401-425.
[5] G. Wang, H. Wang, Y. Ling, Y. Tang, X. Yang, R.C. Fitzmorris, C. Wang, J.Z. Zhang, Y. Li, Nano letters, 11 (2011) 3026-3033.
[6] A.A. Nada, M.F. Bekheet, R. Viter, P. Miele, S. Roualdes, M. Bechelany, Applied Catalysis B: Environmental, 251 (2019) 76-86.
[7] I. Cesar, A. Kay, J.A. Gonzalez Martinez, M. Grätzel, Journal of the American Chemical Society, 128 (2006) 4582-4583.
[8] Y.-S. Hu, A. Kleiman-Shwarsctein, A.J. Forman, D. Hazen, J.-N. Park, E.W. McFarland, Chemistry of Materials, 20 (2008) 3803-3805.
[9] Y. Lin, G. Yuan, S. Sheehan, S. Zhou, D. Wang, Energy & Environmental Science, 4 (2011) 4862-4869.
[10] K. Sivula, F. Le Formal, M. Grätzel, ChemSusChem, 4 (2011) 432-449.
[11] H. Wang, T. Lindgren, J. He, A. Hagfeldt, S.-E. Lindquist, The Journal of Physical Chemistry B, 104 (2000) 5686-5696.
[12] E.M. Fortunato, P.M. Barquinha, A. Pimentel, A.M. Gonçalves, A.J. Marques, L.M. Pereira, R.F. Martins, Advanced Materials, 17 (2005) 590-594.
[13] F.H. Alshammari, P.K. Nayak, Z. Wang, H.N. Alshareef, ACS applied materials & interfaces, 8 (2016) 22751-22755.
[14] A. Tsukazaki, A. Ohtomo, T. Onuma, M. Ohtani, T. Makino, M. Sumiya, K. Ohtani, S.F. Chichibu, S. Fuke, Y. Segawa, Nature materials, 4 (2005) 42.
[15] T. Pauporté, O. Lupan, J. Zhang, T. Tugsuz, I. Ciofini, F.d.r. Labat, B. Viana, ACS applied materials & interfaces, 7 (2015) 11871-11880.
[16] R. Pietruszka, R. Schifano, T.A. Krajewski, B.S. Witkowski, K. Kopalko, L. Wachnicki, E. Zielony, K. Gwozdz, P. Bieganski, E. Placzek-Popko, Solar Energy Materials and Solar Cells, 147 (2016) 164-170.
[17] Y. Tian, C. Hu, Y. Xiong, B. Wan, C. Xia, X. He, H. Liu, The Journal of Physical Chemistry C, 114 (2010) 10265-10269.
[18] L.K. Jagadamma, M. Al-Senani, A. El-Labban, I. Gereige, G.O. Ngongang Ndjawa, J.C. Faria, T. Kim, K. Zhao, F. Cruciani, D.H. Anjum, Advanced Energy Materials, 5 (2015) 1500204.
[19] Z. Balevicius, A. Paulauskas, I. Plikusiene, L. Mikoliunaite, M. Bechelany, A. Popov, A. Ramanavicius, A. Ramanaviciene, Journal of Materials Chemistry C, 6 (2018) 8778-8783.
[20] R. Viter, M. Savchuk, N. Starodub, Z. Balevicius, S. Tumenas, A. Ramanaviciene, D. Jevdokimovs, D. Erts, I. Iatsunskyi, A. Ramanavicius, Sensors and Actuators B: Chemical, 285 (2019) 601-606.
[21] R. Viter, K. Kunene, P. Genys, D. Jevdokimovs, D. Erts, A. Sutka, K. Bisetty, A. Viksna, A. Ramanaviciene, A. Ramanavicius, Macromolecular Chemistry and Physics, (2019).
[22] S.B.A. Hamid, S.J. Teh, C.W. Lai, Catalysts, 7 (2017) 93.
[23] S. Shet, K.-S. Ahn, R. Nuggehalli, Y. Yan, J. Turner, M. Al-Jassim, Thin Solid Films, 519 (2011) 5983-5987.
[24] X. Yang, A. Wolcott, G. Wang, A. Sobo, R.C. Fitzmorris, F. Qian, J.Z. Zhang, Y. Li, Nano letters, 9 (2009) 2331-2336.
[25] X. Zhang, J. Qin, Y. Xue, P. Yu, B. Zhang, L. Wang, R. Liu, Scientific reports, 4 (2014) 4596.
[26] A. Abdulagatov, Y. Yan, J. Cooper, Y. Zhang, Z. Gibbs, A. Cavanagh, R. Yang, Y. Lee, S. George, ACS applied materials & interfaces, 3 (2011) 4593-4601.

[27] H. Gerischer, Journal of Electroanalytical Chemistry and Interfacial Electrochemistry, 82 (1977) 133-143.
[28] C. Jiang, S.J. Moniz, M. Khraisheh, J. Tang, Chemistry–A European Journal, 20 (2014) 12954-12961.
[29] I. Ji, M.-J. Park, J.-Y. Jung, M.-J. Choi, Y.-W. Lee, J.-H. Lee, J.-H. Bang, Bulletin of the Korean Chemical Society, 33 (2012) 2200-2206.
[30] S.K. Karuturi, C. Cheng, L. Liu, L.T. Su, H.J. Fan, A.I.Y. Tok, Nano Energy, 1 (2012) 322-327.
[31] C. Cheng, H. Zhang, W. Ren, W. Dong, Y. Sun, Nano Energy, 2 (2013) 779-786.
[32] M. Liu, C.-Y. Nam, C.T. Black, J. Kamcev, L. Zhang, The Journal of Physical Chemistry C, 117 (2013) 13396-13402.
[33] M. Kulmas, L. Paterson, K. Höflich, M.Y. Bashouti, Y. Wu, M. Göbelt, J. Ristein, J. Bachmann, B. Meyer, S. Christiansen, Advanced Functional Materials, 26 (2016) 4882-4889.
[34] M. Nasr, R. Viter, C. Eid, R. Habchi, P. Miele, M. Bechelany, Surface and Coatings Technology, 343 (2018) 24-29.
[35] M. Weber, A. Julbe, A. Ayral, P. Miele, M. Bechelany, Chemistry of Materials, 30 (2018) 7368-7390.
[36] T. Wang, Z. Luo, C. Li, J. Gong, Chemical Society Reviews, 43 (2014) 7469-7484.
[37] V. Sharma, P. Kumar, J. Shrivastava, A. Solanki, V. Satsangi, S. Dass, R. Shrivastav, Journal of materials science, 46 (2011) 3792-3801.
[38] N. Tarwal, P. Patil, Electrochimica Acta, 56 (2011) 6510-6516.
[39] M. Yousefi, M. Amiri, R. Azimirad, A. Moshfegh, Journal of Electroanalytical Chemistry, 661 (2011) 106-112.
[40] S. Shinde, C. Bhosale, K. Rajpure, Journal of Photochemistry and Photobiology B: Biology, 120 (2013) 1-9.
[41] S. Shinde, A. Korade, C. Bhosale, K. Rajpure, Journal of Alloys and Compounds, 551 (2013) 688-693.
[42] A. Mahroug, S. Boudjadar, S. Hamrit, L. Guerbous, Materials Letters, 134 (2014) 248-251.
[43] M. Salem, S. Akir, T. Ghrib, K. Daoudi, M. Gaidi, Journal of Alloys and Compounds, 685 (2016) 107-113.
[44] D. Dridi, L. Bouaziz, M. Karyaoui, Y. Litaiem, R. Chtourou, Journal of Materials Science: Materials in Electronics, 29 (2018) 8267-8278.
[45] K. Omri, A. Bettaibi, K. Khirouni, L. El Mir, Physica B: Condensed Matter, 537 (2018) 167-175.
[46] C.H. Ahn, J.H. Kim, H.K. Cho, Journal of the Electrochemical Society, 159 (2012) H384-H387.
[47] M. Ahmad, E. Ahmed, Z. Hong, Z. Iqbal, N. Khalid, T. Abbas, I. Ahmad, A. Elhissi, W. Ahmed, Ceramics International, 39 (2013) 8693-8700.
[48] Y. Geng, Z.-Y. Xie, W. Yang, S.-S. Xu, Q.-Q. Sun, S.-J. Ding, H.-L. Lu, D.W. Zhang, Surface and Coatings Technology, 232 (2013) 41-45.
[49] B. Alfakes, J.E. Villegas, H. Apostoleris, R.S. Devarapalli, S.R. Tamalampudi, J. Lu, J. Viegas, I. Almansouri, M. Chiesa, The Journal of Physical Chemistry C, (2019).
[50] P.E. Larson, M.A. Kelly, Journal of Vacuum Science & Technology A: Vacuum, Surfaces, and Films, 16 (1998) 3483-3489.
[51] N.S. Rajput, S.-G. Kim, J.B. Chou, J. Abed, J. Viegas, M. Jouiad, MRS Advances, 1 (2016) 825-830.
[52] B.R. Strohmeier, D.M. Hercules, Journal of Catalysis, 86 (1984) 266-279.
[53] D. Langer, C. Vesely, Physical Review B, 2 (1970) 4885.
[54] J.C. Klein, D.M. Hercules, Journal of catalysis, 82 (1983) 424-441.
[55] P. Wehner, P. Mercer, G. Apai, Journal of Catalysis, 84 (1983) 244-247.
[56] R. Nyholm, A. Berndtsson, N. Martensson, Journal of Physics C: Solid State Physics, 13 (1980) L1091.
[57] T.-C. Tien, L.-C. Lin, L.-S. Lee, C.-J. Hwang, S. Maikap, Y.M. Shulga, Journal of Materials Science: Materials in Electronics, 21 (2010) 475-480.
[58] S.-Y. Pung, K.-L. Choy, X. Hou, C. Shan, Nanotechnology, 19 (2008) 435609.

[59] F. Ghahramanifard, A. Rouhollahi, O. Fazlolahzadeh, Superlattices and Microstructures, 114 (2018) 1-14.
[60] S. Hamrouni, M. AlKhalifah, M. El-Bana, S. Zobaidi, S. Belgacem, Applied Physics A, 124 (2018) 555.
[61] J. Tang, J. Fabbri, R.D. Robinson, Y. Zhu, I.P. Herman, M.L. Steigerwald, L.E. Brus, Chemistry of materials, 16 (2004) 1336-1342.
[62] C.-K. Lee, E. Cho, H.-S. Lee, C.S. Hwang, S. Han, Physical Review B, 78 (2008) 012102.
[63] L. Cai, F. Ren, M. Wang, G. Cai, Y. Chen, Y. Liu, S. Shen, L. Guo, international journal of hydrogen energy, 40 (2015) 1394-1401.
[64] A.N. Birgani, M. Niyaifar, A. Hasanpour, Journal of Magnetism and Magnetic Materials, 374 (2015) 179-181.
[65] S.-H. Ko Park, Y.E. Lee, Journal of materials science, 39 (2004) 2195-2197.
[66] A.U. Pawar, C.W. Kim, M.J. Kang, Y.S. Kang, Nano Energy, 20 (2016) 156-167.
[67] J. Tauc, R. Grigorovici, A. Vancu, physica status solidi (b), 15 (1966) 627-637.
[68] B.D. Viezbicke, S. Patel, B.E. Davis, D.P. Birnie III, physica status solidi (b), 252 (2015) 1700-1710.
[69] F. Urbach, Physical Review, 92 (1953) 1324.
[70] K.V. Bangera, C. Anandan, G. Shivakumar, Journal of Alloys and Compounds, 578 (2013) 613-619.
[71] M. Caglar, S. Ilican, Y. Caglar, Thin Solid Films, 517 (2009) 5023-5028.
[72] S.K. O'Leary, S. Zukotynski, J.M. Perz, Journal of non-crystalline solids, 210 (1997) 249-253.
[73] C. Garlisi, C.-Y. Lai, L. George, M. Chiesa, G. Palmisano, The Journal of Physical Chemistry C, 122 (2018) 12369-12376.
[74] S.A. Ansari, M.M. Khan, S. Kalathil, A. Nisar, J. Lee, M.H. Cho, Nanoscale, 5 (2013) 9238-9246.
[75] S. Anandan, N. Ohashi, M. Miyauchi, Applied Catalysis B: Environmental, 100 (2010) 502-509.
[76] K.-S. Ahn, Y. Yan, S. Shet, T. Deutsch, J. Turner, M. Al-Jassim, Applied physics letters, 91 (2007) 231909.
[77] T. Käämbre, M. Vanags, R. Pärna, V. Kisand, R. Ignatans, J. Kleperis, A. Šutka, Ceramics International, 44 (2018) 13218-13225.
[78] F. Rasouli, A. Rouhollahi, F. Ghahramanifard, Superlattices and Microstructures, 125 (2019) 177-189.
[79] R. Beranek, Advances in Physical Chemistry, 2011 (2011).
[80] L. Liu, Z. Mei, A. Tang, A. Azarov, A. Kuznetsov, Q.-K. Xue, X. Du, Physical Review B, 93 (2016) 235305.
[81] J. Kaupužs, A. Medvids, P. Onufrijevs, H. Mimura, Optics & Laser Technology, 111 (2019) 121-128.
[82] S.Y. Chiam, M.H. Kumar, P.S. Bassi, H.L. Seng, J. Barber, L.H. Wong, ACS applied materials & interfaces, 6 (2014) 5852-5859.
[83] T. Lopes, L. Andrade, F. Le Formal, M. Gratzel, K. Sivula, A. Mendes, Physical Chemistry Chemical Physics, 16 (2014) 16515-16523.
[84] B.H. Meekins, P.V. Kamat, ACS nano, 3 (2009) 3437-3446.
[85] R. Freitas, M. Santanna, E. Pereira, Electrochimica Acta, 136 (2014) 404-411.
[86] D.n. Monllor-Satoca, R. Gómez, W. Choi, Environmental science & technology, 46 (2012) 5519-5527.
[87] Q. Cheng, M.K. Benipal, Q. Liu, X. Wang, P.A. Crozier, C.K. Chan, R.J. Nemanich, ACS applied materials & interfaces, 9 (2017) 16138-16147.
[88] S. Hu, N.S. Lewis, J.W. Ager, J. Yang, J.R. McKone, N.C. Strandwitz, The Journal of Physical Chemistry C, 119 (2015) 24201-24228.
[89] C. Li, T. Wang, Z. Luo, D. Zhang, J. Gong, Chemical Communications, 51 (2015) 7290-7293.